02,05

External and internal demanetizing fields as one of the main fundamental reasons for the low density of critical current in twinned $YBa_2Cu_3O_{7-x}$ high-temperature superconductors

© H.R. Rostami

Fryazino Branch, Kotel'nikov Institute of Radio Engineering and Electronics, Russian Academy of Sciences, Fryazino, Moscow oblast, Russia

E-mail: rostami@ms.ire.rssi.ru

Received June 27, 2023
Revised June 27, 2023
Accepted July 10, 2023

An oscillatory differential method of local approximation is applied to study the effect of local internal and external demagnetizing fields on the density of the critical current J_c of intertwin Josephson weak links in YBCO HTSC samples. Demagnetizing fields $YBa_2Cu_3O_{7-x}$ of samples with different J_c and twin size J_c are measured in the d and H_D modes. The following parameters are determined: the twin size d, the thermodynamic first critical magnetic fields of twins H_{ic1}, the demagnetizing fields of twins H_{ic1}, the densities of intertwin effective critical currents H_{Dtr}, the critical pinning currents J_{ceff}, and the Meissner screening critical currents J_{cp}. It is shown that, at the fields H_{ic1}, large twins are stepwise decomposed into a group of smaller twins with close demagnetizing factors. It is found that an increase in J_{cg} and J_{ceff} and a decrease in d lead, on the one hand, to a decrease in J_c due to an increase in H_D and H_{Dtr} produced by J_{ceff} and J_{cg}, on the other hand, to an increase in J_{ceff} and J_{cg} due to a decrease in d. For samples with large J_c and d, as well as for samples with low values of J_c and d in a field of about $\sim 8 \cdot 10^{-2}$ T, H_D, H_{Dtr} and J_c suppress by ~ 70 about $\sim 60\%$, respectively. According to the results obtained in the present study and the known literature data, d decreases with increasing d; in this case, a decrease in d leads to a decrease, rather than an increase, in J_c. Since the weak links and low values of J_c are fundamental properties of HTSCs, the literature data should be corrected with regard to the important facts on the effect of H_D and H_{Dtr} on J_c.

Keywords: twins, monodomains, crystallites, grains, sub- and nanocrystallites, demagnetizing fields, magnetic flux trapping, critical currents.

DOI: 10.61011/PSS.2023.09.57106.126

1. Introduction

Currently, high-temperature superconducting (HTSC) epitaxial films $REBa_2Cu_3O_7$ (REBCO, where RE is the rare earth element) and conductors with $REBa_2Cu_3O_7$ coating with extremely high critical currents $J_c \approx 5 \cdot 10^9 - 10^{10}$ A/m^2 have been developed by creating strong pinning centers. However, despite the achieved success, the obtained critical currents are still much lower than the Ginzburg–Landau depairing critical current ($J_c^{GL} \approx 10^{13}$ A/m^2). With depletion of capabilities for increase of J_c in HTSC materials only using the pinning technique, search for other fundamental causes behind limitation of J_c in the HTSC materials becomes apparent. Identification of new issues and search for other technological practices to ensure additional increase of J_c in HTSC materials up to J_c^{GL} and their proper interpretation will be of great importance for physics, electronics, electric and magnetic power engineering. For more technologically available $YBa_2Cu_3O_{7-x}$ (YBCO), it has been found that even the most perfect YBCO single crystals contain a lot of regularly arranged twin boundaries (TB) with twinning plane (110). Depending on the method of material preparation, TB width can be $\Delta d \approx (30-50) \cdot 10^{-10}$ m and the distance between TBs can be $d \approx (200-2000) \cdot 10^{-10}$ m [1,2]. This relation between parameters makes the physical properties of layered HTSC materials highly sensitive to minor spatial inhomogeneities, since their coherence length is of the same order of magnitude as the TB width, interlayer, interatomic and interelectronic distances [2,3]. It should be noted that the presence of TB is inherent in the very nature of YBCO HTSC, since twin domains form as a result of the structural phase transition from the tetragonal (nonsuperconducting) phase to the orthorhombic (superconducting) phase at ~ 700°C and/or as a result of varying stoichiometry of samples induced by doping [4,5]. Since the properties of TB are also vividly pronounced in other cuprates (better in LaSrCuO) and iron pnictides (twin, rhombic, underdoped $Ba(Fe_{1-x}Co_x)_2As_2$crystals) [6], it will be impossible to remove TB and they cannot be ignored. On the other hand, as mentioned above, HTSC materials have a complex crystal structure consisting of twins (monodomains, crystalline grains, sub- and nanocrystallites) interconnected by weak Josephson couplings. This results in high dependence of the magnetic transport properties of HTSC materials on the density of a network of weak couplings that „cut“ them, in particular, on the density

and the spatial distribution of TB. It is shown in [3,7] that the HTSC sample is abruptly „separated“ into twin groups with quantum spatial scales in a stepwise manner with the growth of the external magnetic fields due to suppression of intertwin Josephson critical currents and weak couplings with external and internal local demagnetization fields. As a result of the development of such scenario, the twin groups that occur during the sample „separation“ are also sorted by demagnetizing factors n. Due to high intratwin current level, the magnetic response signal level is increased, because the sensor face simultaneously covers a lot of twins with close n, which are contained in each twin group. In addition, as a result of separation of the sample into twins, linear dimensions of the twins decrease stepwise and become much smaller than λ — magnetic field penetration depth into the sample and its twins [3,7]. According to the existing situation, questions arise of whether the currently available corrected analytical [8] and generalized [9] Bean critical state models [10] for type-II hard superconductors, which can adequately describe the flux profile and current density distributions in the sample, can be reasonably applied to HTSC materials and whether J_c can be unambiguously determined from the experimental findings. With the growth of the field, YBCO HTSC get separated in a stepwise manner into smaller twins with strengthened weak intertwin couplings, and increasing intertwin and intratwin critical currents. Therefore, n varies during filed penetration into the sample and twins, and it is necessary to study the magnetic field dependence of the sample's effective demagnetizing factor $n_{\text{eff}}(H_o)$ (see below) in order to describe the magnetic properties of HTSC materials and physical processes in the Josephson medium. In addition, no study has been performed so far to investigate the influence on the intertwin critical current density J_c induced by the demagnetization fields of the sample (H_D) and its twins (H_{Dtr}) generated by the Meissner critical image twin currents (J_{cg}), intratwin critical pinning currents (J_{cp}) and effective critical twin currents (J_{ceff}). Therefore, the fundamental values of the first (H_{c1}) and second (H_{c2}) critical magnetic fields and practically relevant J_c, that play an extremely important role in type-II superconductor electrodynamics, without considering sample's $J_c(H_D)$ and twins' $J_c(H_{Dtr})$, can be sufficiently correctly determined using magnetic and magnetic transport methods for isotropic (with cubic symmetry of the crystal lattice) long cylindrical or endless flat samples of homogeneous superconductors with the surface parallel to the magnetic field. Even when the twin distribution functions by shape, dimensions, mutual arrangement and orientation are restored using the X-ray or neutron diffraction study results, it is highly unlikely that valid information regarding H_{c1}, H_{c2}, J_c can be obtained without considering the sample's $J_c(H_D)$ and twins $J_c(H_{Dtr})$. Thus, considering the governing role of H_D and H_{Dtr} in formation of macroscopic parameters of polycrystalline HTSC materials, the equations representing the critical state model shall be corrected and numerically simulated during the model construction process. When there is information regarding the magnitude of $J_c(H_D)$ and $J_c(H_{Dtr})$, their dependence on the external field, temperature, dimensions and spatial distribution of twins, it is possible to find the value, spatial distribution, field and temperature dependence of the thermodynamic field H_i [3,7]. This, in turn, will help create a generalized analytical model of a uniformly magnetized sample to allow adequate description of spatial distributions of flux profile and current density in the HTSC sample. Construction of such model is essential for deeper understanding of physical processes taking place in the sample, twins and Josephson medium as a whole. Moreover, J_c can be unambiguously determined from the experimental results, J_c calculation procedure can be simplified and calculation accuracy can be increased.

2. Experimental methods and samples

2.1. Experiment details

The foregoing investigations were carried out using oscillatory differential procedure of local approximation offered before to study the features of interaction between the crystalline and magnetic microstructures of superconductors. The procedure developed on a conceptually new physical basis can expose the sample to the oscillating evanescent local magnetic field with stepwise amplitude and frequency adjustment. By local approximation to the magnetic response space and by differential signal recording method, it is possible to identify the vortex and Meissner region interface experimentally and to study the distribution of internal local demagnetization fields in YBCO HTSC in vicinity and on TB. The developed precision oscillatory differential procedure of local approximation [3,7] is based on the recording of H_D and H_{Dtr}, which are caused by the trapped flux and occur only from the oscillating local evanescent magnetic field front. For this, capacity $(C \approx 2.5 \cdot 10^{-8}\,\text{F})$ is included in parallel to the solenoid generating the external field with inductance $L \approx 4.22\,\text{Hn}$ and winding resistance $R \approx 92.6\,\Omega$ at 77.4 K. After application of DC voltage to the formed LC-circuit, oscillating local evanescent magnetic field $H(t) = H_o \exp(-\beta t)\cos\Omega t$ occurred in the solenoid. In this expression $\beta = R/(2L) \approx 22\,\text{s}^{-1}$ is the extinction coefficient, $\Omega = (\omega^2 - \beta^2)^{1/2} \approx 352\,\text{Hz}$ is the natural frequency of the oscillating circuit, $\omega^2 = 1/(LC)$. Since the oscillation amplitude $H_o \exp(-\beta t)$ from H_o to $-H_o$ decayed exponentially to zero, the flux was not trapped from the variable field and trapping was recorded only from field H_o. The maximum amplitude of the oscillating local evanescent magnetic field achieved $\sim 8 \cdot 10^{-2}\,\text{T}$ and varied stepwise with step $\Delta H_o \approx 4.66 \cdot 10^{-4}\,\text{T}$.

$H_D(H_o)$ was studied using the offered procedure in zero field cooling (ZFC) mode and zero field cooling mode with magnetic flux accumulation (ZFCMFA) as follows:

a) ZFC mode — the sample was cooled to the liquid nitrogen temperature in zero magnetic field, then an external magnetic field step was applied and H_D was measured after

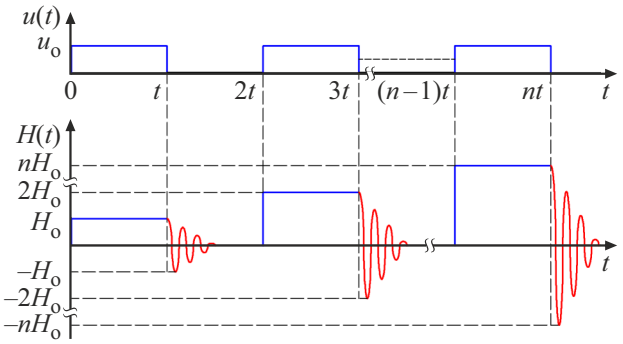

Figure 1. Unit operation time diagram for random L and C of LC circuit showing the oscillating local evanescent magnetic field generation process in the ZFC and ZFCMFA modes. To simplify the findings analysis procedure, the step size was steadily increased stepwise by an equal value at equal time intervals t.

300 s on the surface in the center of the sample. Then the sample was heated above T_c and the experiment was repeated for another ΔH_o.

b) The ZFCMFA mode differs from the ZFC mode in that after the initial trapping without varying H_D and without sample heating the next field step ΔH_o was applied and after 300 s the total H_D was measured, etc.

In the ZFC mode, direct interaction is provided between the magnetic field and sample in the Meissner state and, thus, the macroscopic properties of the sample are studied. Since in the ZFCMFA mode, the flux from the previous step has been already frozen in the sample, then stepwise suppression of the weak coupling currents is performed by the scattering fields of the previously trapped vortices in the sample and interaction between the external field and separated twins is provided as far as possible [3,7]. Thus, in contrast to the ZFC mode, the ZFCMFA mode allows to examine physical processes within the sample, in addition to the macroscopic HTSC properties.

Figure 1 contains the unit operation time diagram for random $L$and $C$of the LC circuit showing the oscillating local evanescent magnetic field generation process in the ZFC and ZFCMFA modes. To simplify the findings analysis procedure, the step size was steadily increased stepwise by an equal value at equal time intervals. Spatial resolutions of the applicable procedures and measurement accuracy also depend on the step application time and the time between the release of the oscillating local evanescent magnetic field step and the start of measurement, since the influence of relaxation processes (time of flux entry/exit in/from the sample) on the measurement decreases with growing t. Generally, within $t = 300$ s, the quickly relaxing portion of the trapped flux density is ended and a „rigidly" fixed vortex lattice is set in the sample. By subtraction of H_{D2}measured in the ZFCMFA mode from H_{D1} measured in the ZFC mode, the influence on the surface barrier, boundary and volumetric pinning measurements in the sample and twins was avoided. Such procedure together with the stepwise amplitude change ΔH_o of the oscillating local evanescent magnetic field applied to the sample allows to perform transition from the Gaussian to δ-like spatial distribution of H_{Dtr}. Moreover, differentiation of the magnetic field dependence $[(H_{D1} - H_{D2})/\Delta H_o](H_o)$ carried out in this way allows to detect the stepwise change of $\Delta H_{Dtr}/\Delta H_o$ derivative in the field region when the vortex and Meissner region interface intersects TB. This considerably reduces the width of the σ-like distribution and more accurately emphasizes the components associated with the Meissner image currents of the sample and its twins. Thus, TB may be separated from the weak Josephson grain couplings and detect not only extended TB, but also small TB masked from the long grain couplings, dislocations and other defects side. To ensure smooth transition from large to small spatial scales, the field step height ΔH_o was gradually reduced to the minimum value after each measurement cycle, for this the sample was heated to a temperature higher than T_c and then cooled again to $T = 77.4$ K. Such approach allowed to mode the magnetic field front stepwise inside the sample, twins and backwards. This, in turn, allowed to follow the movement of the vortex and Meissner region interface. Since under the experiment condition the influence of the trailing edge of the oscillating local evanescent magnetic field was avoided, then probing of the sample volume using the variable evanescent magnetic field front allowed to study separately the magnetic state of regions with the same critical parameters, perform „local" flux trapping and change the topology of the trapped flux using the field front and gradually, with the external field growth, localize the vortex and Meissner region interface around the twins with the highest critical parameters (H_{c1i}, J_{ci}, T_{ci}). This allows to separate small-angle and large-angle grain boundaries selectively. Thus, it is also possible to get useful information about the magnetic properties of samples depending on the crystallographic microstructure of such spatially inhomogeneous superconductors, which include HTSC materials.

$H_D(H_o)$ was studied at the liquid nitrogen temperature (77.4 K) using Hall effect transducers (HT) with the working zone dimensions $(0.1 \times 0.05)10^{-6}$ m^2 and transduction factors $\sim 0.12\,\mathrm{V}\cdot\mathrm{T}^{-3}$. To measure $H_D(H_o)$, one of HT_1 was installed in the geometrical axis center on the sample surface and the second HT_2 is installed in the undisturbed field far from the sample. Both HTs had close specifications, were on the same plane and in opposite-phase coupling. The HT transduction factors were aligned by means of independent current adjustment via HT_2. To avoid the influence of spurious current field through HT_1 on the measurements, current was applied through double wound wires with small wrapping pitch. The second of the copper wires was adhered in the center on the back side of the HT_1 pad and was energized separately from the adjustable power supply. The unit allowed to record the HT signal with an accuracy of at least $2.5 \cdot 10^{-7}$ T and to move HT from the center along the z axis and to the sample perophery [11,12]. The magnetic field was perpendicular to the sample plane.

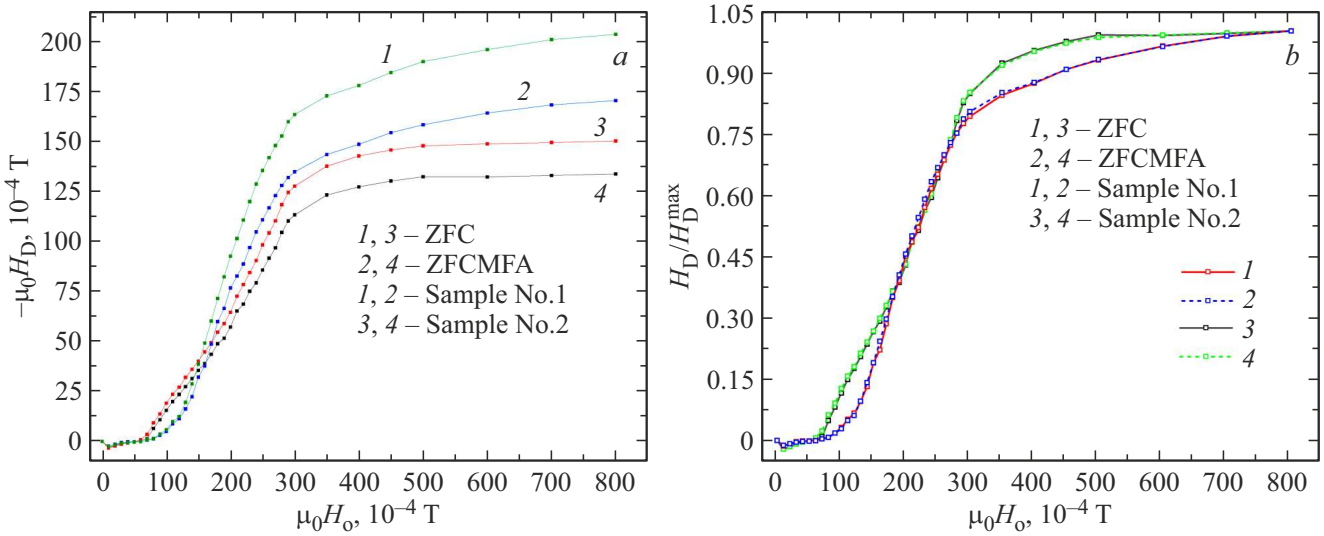

Figure 2. *a*) Typical magnetic field dependences $H_D(H_o)$. *b*) Standardized $(H_D/H_D^{max})(H_o)$. Curves *1* and *2* are for sample No. 1, curves *3* and *4* are for sample No. 2. Curves *1* and *3* were measured in the ZFC mode, curves *2* and *4* were measured in the ZFCMFA mode. Temperature $T \approx 77.4$ K. (μ_0 is the magnetic constant.)

The terrestrial field component H_z was compensated by a coil coaxial to the solenoid producing the external magnetic field.

2.2. Samples

For comparative analysis, the investigations were carried out on YBCO samples with different thicknesses, microstructures and edge barrier heights, volumetric pinning, demagnetization and J_c. The thickness of the disc-shaped samples with diameter $\sim 8 \cdot 10^{-3}$ m made from bulk textured (c axis is perpendicular to the sample plane) quasi-single-crystalline and polycrystalline YBCO was equal to $\sim (0.7-4.2) \cdot 10^{-3}$ m. $T_c \approx 92$ K and $\Delta T_c \approx 1$ K were obtained from temperature dependence of inductance $\ell(T)$ for quasi-single-crystalline and polycrystalline YBCO samples. The critical temperature was measured using a resonance inductance meter with a sensitivity of $\sim 10^{-6}$ Hn in the frequency range of $(355-505) \cdot 10^3$ Hz with the temperature dependence of the microsolenoid inductance $\ell(T)$, where $\ell \approx 6.5 \cdot 10^{-5}$ Hn. The quasi-single-crystalline and polycrystalline samples were cut from a cylindrical blank. End surfaces were removed with a diamond cutter to avoid oxygen distribution inhomogeneity at ends relative to the interior. Fused textured quasi-single-crystalline YBCO samples were synthesized using a seed placed on top at high temperature. The microscopic examination showed glossy (single-crystalline) blocks with size $\sim 10^{-5}$ m^2 separated by narrow green inclusions on the perimeter and on the well polished surface. This proved that the trapped flux was mapped using HT. The critical current was measured using a four-probe arrangement on bars with cross-section $\sim (0.7 \times 0.7) \cdot 10^{-6}$ m^2 cut from the same blanks and ground through the thickness and width. Contacts were applied using silver paste. polycrystalline textured YBCO samples with a radius of $R \approx 4 \cdot 10^{-3}$ m and thickness $h \approx 0.7 \cdot 10^{-3}$ m with average twin size $\sim 10^{-6}$ m had $J_c \approx 6.5 \cdot 10^6$ A/m^2 (sample No. 1). Quasi-single-crystalline textured YBCO samples with a radius of $\sim 4 \cdot 10^{-3}$ m and thickness of $\sim 0.7 \cdot 10^{-3}$ m had $J_c \approx 4.5 \cdot 10^6$ A/m^2 (sample No. 2).

3. Results

Figure 2 shows for samples No. 1 and 2 a) magnetic sample field dependences $H_D(H_o)$ and b) dependences standardized to the maximum demagnetization field $(H_D/H_D^{max})(H_o)$. Curves *1* and *2* correspond to sample No. 1, curves *3* and *4* correspond to sample No. 2. Curves *1* and *3* were measured in the ZFC mode, curves *2* and *4* were measured in the ZFCMFA mode. According to Figure 2, *a*, in weak fields curves *1–4* grow weakly, after field values $H_{c1} \approx 70 \cdot 10^{-4}$ T (curve *1*) and $H_{c1} \approx 60 \cdot 10^{-4}$ T (curve *3*) curves *1–4* start growing sharply and gradually achieve saturation in the strong field region. Curves *1* and *3* grow faster that curves *2* and *4*. Dependences $H_D(H_o)$ shown in Figure 2, for sample No. 1 (curves *1* and *2*) and for sample No. 2 (curves *3* and *4*), allow to separate twins' H_{Dtr} and sample's H_D caused by the sample surface currents J_c. On the other hand, as shown in Figure 2, *b*, on dependences $(H_D/H_D^{max})(H_o)$, curves *1* and *2* for sample No. 1 as well as curves *3* and *4* for sample No. 2 are almost merged, while curves *3* and *4* achieve the saturation region faster than curves *1* and *2*. As will be shown below, such result shows that the local demagnetization fields in the presence of the external magnetic field are generally generated by current J_{cg} and without field — by current J_{cp}, because the density of the

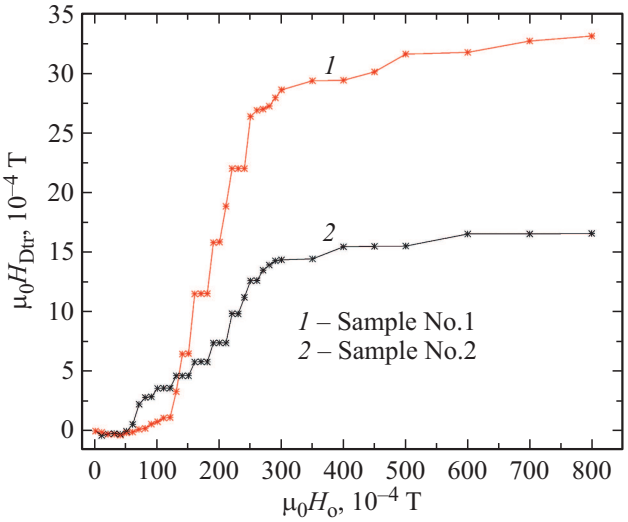

Figure 3. Magnetic field dependences of the twin demagnetization fields $H_{Dtr}(H_o)$ reflecting the difference of curves *1* and *2* from Figure 2, *a* (curve *1*) and *3*, and *4* from Figure 2, *a* (curve *2*). $T = 77.4$ K.

Meissner critical image currents J_{cg} of twins is more than two orders of magnitude greater than the density of the critical twin pinning currents J_{cp} and is approximately five orders of magnitude greater than the density of the intratwin critical rms currents J_{ceff}.

For samples No. 1 and 2, Figure 3 shows the magnetic field dependences of the twin demagnetization fields $H_{Dtr}(H_o)$ reflecting the difference behavior $H_{Dtr} = H_{D1} - H_{D2}$ depending on the field. Curve *1* corresponds to the difference of curves *1* and *2* for sample No. 1, curve *2* corresponds to the difference of curves *3* and *4* for sample No. 2. Figure 3 shows the occurrence of jumps on curves *1* and *2* with thermodynamic first critical magnetic fields of twins (H_{ic1}). H_{ic1} this field is inside the sample and can be calculated from $H_{ic1} = H_o/(1 - n_{eff})$, where n_{eff} describes the variation of n as the field penetrates the sample. The oscillation differential method of local approximation described above allows to separate selectively the vortex and Meissner region interface and to enhance the TB manifestation. As shown in [3,7], the vortex and Meissner region interface, in turn, is n_{eff}.

Figure 4, *a* shows magnetic field dependences $H_{ic1}(H_o)$ for sample No. 1 (curve *1*) and for sample No. 2 (curve *2*). As shown in Figure 4, *a*, H_{ic1} grows with the field growth; this is caused by growth of J_{cg} of these twins and decrease of their n with the sample disintegration into smaller twins, as result of which field penetration into the sample becomes more complicated.

Density of the Meissner critical image currents J_{cg} of twins can be calculated using expression [13]:

$$J_{cg} = 10H_c/(4\pi\lambda). \quad (1)$$

Figure 4, *b* shows magnetic field dependences $J_{cg}(H_{ic1})$ in the semilogarithmic scale for samples No. 1 (curve *1*) and No. 2 (curve *2*). Points on curves *1* and *2* correspond to J_{cg} values calculated for typical H_{ic1} values at which irregularities occur on curves *1* and *2* Figure 3. As shown in Figure 4, *b*, the Meissner critical image currents are linearly dependent on the field. Such result is associated with the fact that in the weak field region (fast growth occurs after flux penetration into the sample) the field is mainly concentrated in the intertwin space. Stepwise suppression of the intertwin Josephson critical currents occurs in large circuits consisting of twins interconnected by weak Josephson couplings. Gradual transformation of large circuits into twin clusters and smaller circuits ends with flux penetration in the intertwin space. Then the flux enters inside the twins with higher critical currents and growing during disintegration of twins into smaller twins. Thus, the growth of $J_{cg}(H_{ic1})$ is decelerated. The consistent behavior of dependences$J_{cg}(H_{ic1})$ for samples No. 1 and 2 shows that, although the critical currents of weak couplings increase as twins become smaller, they still are separated into smaller twins. The findings also show that it is the disintegration of the sample into sub- and nanocrystals with small demagnetizing factors that is the cause of weakening influence of the external magnetic field on the critical current and non-zero current flow through the HTSC sample up to very strong magnetic fields.

In order to select a model to determine the density of the critical magnetization rms current of the sample J_{ceff} in the saturation regions occurring after the jumps H_{Dtr} in Figure 3, the following operations were carried out. First, axial distributions of the trapped flux density $[H_{tr}(z)](H_o)$, $[H_{tr}(z)](I)$ were measured and standardized axial distributions $[H_{tr}(z)/H_{tr}(0)](H_o, I)$ were plotted using HT_1 for different oscillating local evanescent magnetic field amplitudes and transport currents flowing perpendicular to the force lines of the oscillating local evanescent magnetic field. Then according to the Biot-Savart law within the Bean model [10], axial distributions and standardized axial distributions were calculated for the constant J_c which does not depend on the current field.

$$H_{tr}(z) = (2\pi/c)J_c \times \{(h+z)\operatorname{arcsin} h[(R/(h+z)] - z \operatorname{arcsin} h(R/z)\}. \quad (2)$$

$$H_{tr}(z)/H_{tr}(0) = [1/h \operatorname{arcsin} h(R/h)] \times \{(h+z)\operatorname{arcsin} h[(R/(h+z)] - z \operatorname{arcsin} h(R/z)\}. \quad (3)$$

Then the axial distributions and standardized axial distributions were calculated according to the Biot-Savart law using the approximated uniformly magnetized sample model.

$$H_{tr}(z) = (2\pi/c)J_c \times \{(h+z)^2/[(h+z)^2 + R^2]^{1/2} - z^2/(z^2+R^2)^{1/2}\}. \quad (4)$$

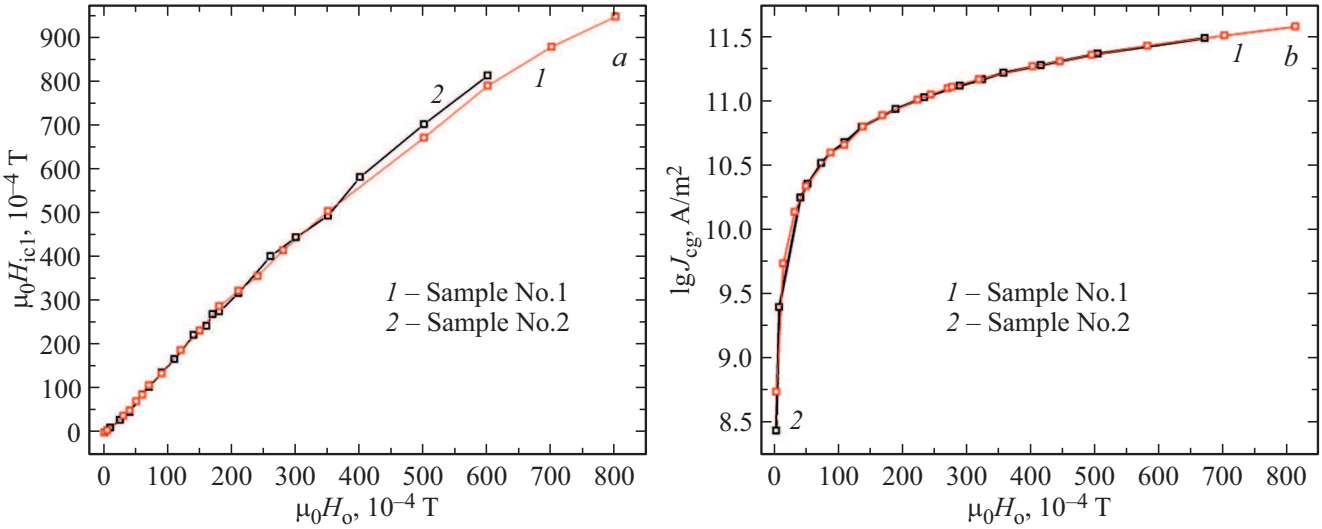

Figure 4. Magnetic field dependences: *a*) of the thermodynamic first critical magnetic field $H_{ic1}(H_o)$ for sample No. 1 (curve *1*) and for sample No. 2 (curve *2*); *b*) dependences $J_{cg}(H_{ic1})$ in the semilogarithmic scale for samples No. 1 (curve *1*) and No. 2 (curve *2*). Points on the curve correspond to J_{cg} values calculated for typical $H_{textic1}$ values at which irregularities occur on curves *1* and *2* Figure 3. $T = 77.4$ K.

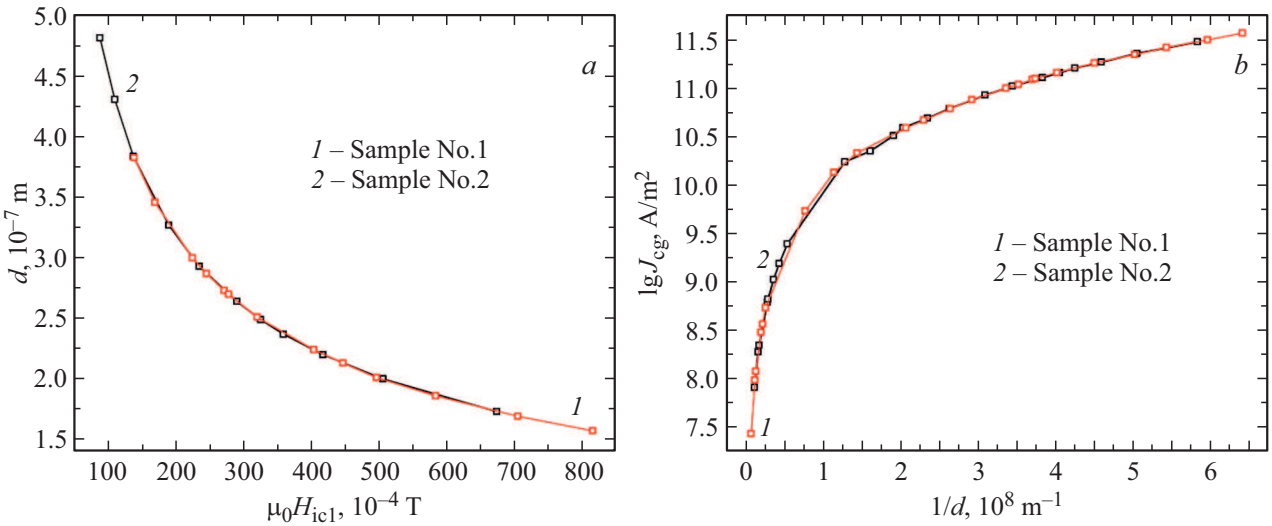

Figure 5. For samples No. 1 and 2, *a*) magnetic field dependence of the linear dimensions of sub- and nanocrystallites d on the typical H_{ic1} values, curve *1* — for sample No. 1, curve *2* — for sample No. 2; *b*) dependences $J_{cg}(1/d)$ are provided. $T = 77.4$ K.

$$H_{tr}(z)/(H_{tr}(0) = [(h^2 + R^2)^{1/2}/h^2] \times \{(h+z)^2/[(h+z)^2 + R^2]^{1/2} - z^2/(z^2 + R^2)^{1/2}\}. \quad (5)$$

Comparison of experimental curves $H_{tr}(z)/H_{tr}(0)$ with the theoretical curves plotted using equations (3) and (5) has shown that the experimental curve in fields $\sim (1-60) \cdot 10^{-4}$ T is well described by equation (3) and in fields $\sim (1-800) \cdot 10^{-4}$ T — by equation (5). When the transport current flows through the sample, increased current also results in failure of weak couplings and $H_{tr}(z)/H_{tr}(0)$ approaches the case of similarly magnetized isolated twins. It should be noted that for comparative analysis we also performed the study using HT with various work surfaces S_{HP}. It has been found that growth of S_{HP} demonstrated greater deviation of $H_{tr}(z)/H_{tr}(0)$ from the Bean model described by equation (3) both during growth and decrease of the distance between the sample surface and HT. With increasing z, field of view is increased and HT starts detecting the varying distribution of twins and vortices from the sample center to the edge. In case of the uniformly magnetized sample model, dependence $H_{tr}(z)/H_{tr}(0)$ calculated using equation (5) and the measured curves, both with growth and decrease of z, fit each other well and remained almost unchanged when HT with different S_{HP} were replaced.

Thus, in the center on the sample surface, we have for $z = 0$ from equation (4)

$$J_{\text{ceff}} = (c/2\pi)H_{\text{Dtr}}(h^2 + R^2)^{1/2}/h^2. \quad (6)$$

Twin sizes can be determined from the following expression

$$d = (\Phi_0/H_{\text{ic1}})^{1/2}, \quad (7)$$

where F_0 is the flux quantum.

As shown in Figure 5, *a*, curves *1* and *2* with the field growth have smooth and monotonous dip, while the linear dimensions of sub- and nanocrystallites d for sample No. 1 decrease from $4.9 \cdot 10^{-7}$ m to $1.8 \cdot 10^{-7}$ m (initial points on the curve are not shown for clarity). Error of estimate d is defined by the spread of sub- and nanocrystallite sizes due to loose parallelism of TB and variability of their constant.

4. Models and discussion

When a bulksuperconductor is placed in a weak external magnetic field, image currents are induced on the sample surface and generate the demagnetization field H_{D} which is oriented against the external magnetic field H_{o} and compensates the external magnetic field inside the sample. It is the field H_{D} that induces field distribution distortion near the superconductor surface. For the ellipsoidal sample $H_{\text{D}} = 4\pi nI$, where $I = M/V$ is the effective magnetization of the sample, M is the magnetic moment of the superconductor generated by the image currents, and V is the sample volume. The higher sample magnetization $4\pi nI$, the stronger demagnetization field H_{D} [14]. By flux trapping in the sample, it is possible to track, with flux growth, the behavior of emerging isolated twin clusters or of similarly magnetized twins not interacting with each or other or their combinations [3,7]. Effective magnetization of twins $I_{\text{geff}} = V_g^{-1}M_{\text{geff}}$ will be defined by rms supercurrents of separate twins $J_{\text{ceff}} = c \cdot \text{rot}M_{\text{geff}}$ (where V_g is the twin volume, M_{geff} is the effective magnetic moment of twins, c is the speed of light).

A model is provided in [3] demonstrating the square-shaped (for convenience) single-domain disintegration into four crystallites, each of them, in turn, is separated into four sub- and nanocrystallites. According to such pattern, in the intersection points of periodically arranged TBs inside the twins, intratwin interface vortices are induced with Abrikosov vortices between them. Pinning currents J_{cp} circulate around them. Also, in TB intersection points in intertwin space, intertwin interface antivortices and Josephson vortices are formed through which scattering fields of the intratwin interface vortices and Abrikosov vortices are closed. The intratwin interface vortices and intertwin interface anivortices clasp the Abrikosov and Josephson vortices and restrict their movement; this is demonstrated by weak relaxation of the trapped flux with gradual reducing to zero with field growth. When the oscillating local evanescent magnetic field is applied,

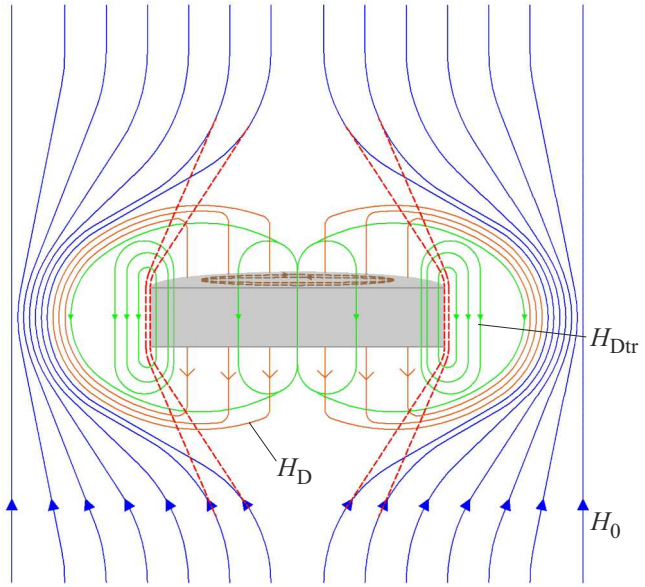

Figure 6. Model explaining the results shown in Figure 2.

reverse currents J_{cg} flow on the twin surfaces and induce demagnetization fields oriented against the demagnetization fields associated with the vortex scattering fields supported by the intratwin currents J_{cp}. Image currents clasp and localize the demagnetization fields in TB and, thus, the resulting fieldH_{Dtr} suppresses the critical currents J_{c} through the intertwin weak couplings and causes disintegration of large twins into smaller isolated uniformly magnetized twins with currents J_{ceff}. After removal of the oscillating local evanescent magnetic field, H_{Dtr} strengthened by localization is „frozen“ according to the self-induction law maintaining the sample in a uniformly magnetized state. Thus,

$$J_{\text{cp}} = J_{\text{cg}} - J_{\text{ceff}}. \quad (8)$$

The model explaining the results shown in Figure 2 can be qualitatively demonstrated using Figure 6. For this, a magnetic barrier for vortices entry from the next field step is formed in the sample in the ZFCMFA mode by initial flux trapping artificially in the form of twin demagnetization fields H_{Dtr}. Further, in order to trap the flux from the next oscillating local evanescent magnetic field step, first compensate the demagnetization fields from the trapped flux density B_{tr2} and remove the magnetic barrier formed before. Then increase magnetic pressure on the Meissner image currents of twins until the sample is disintegrated into the next smaller twin groups with close n. With increasing external magnetic field, finally full compensation of H_{Dtr} occurs and force lines H_{o} approach the sample edges (red dashed lines in Figure 6). According to Figure 2, due to numerous linear and point defects in bulk samples No. 1 and 2, curves *1–4* have no jumps with simultaneous flux penetration into the twins after each twin separation. However, as shown in Figure 3, jumps are clearly visible

on curves *1* and *2* at fields H_{ic1} after differentiation. According to [3,7], for more pure epitaxial YBCO films, jumps are detected on dependences $B_{tr2}(H_o)$ even without differentiation.

Figure 7 shows dependences for samples No. 1 (curve *1*) and No. 2 (curve *2*): *a*) $J_{ceff}(H_{ic1})$; *b*) $J_{ceff}(J_{cg})$ and *c*) $J_{ceff}(1/d)$. Fast growth sections (a–b), (b–c) on curves *1* Figure 7, *a* and *b* correspond to the fact that at high *n* values twins are disintegrated, with field growth, into smaller twin groups with close *n* resulting in fast growth of their H_{ic1}, J_{cg} and, therefore, to the growth of J_{ceff}. On curves *1* Figure 7, *b* and *c*, stepwise growth of J_{ceff} on section (d–e) is also associated with growth of J_{cg} and decrease of *d* after twin disintegration. This was clearly seen during small-pitch field scanning (not shown). The „plateau“ regions on sections (c–d), (e–f) on curves *1* Figure 7, *a* and *b* and sections (c–d), (f–g) in Figure 7, *c*, as well as sections (b′–c′), (d′–e′), (f′–g′) on curves *2* Figure 7, *a*, regions (a′–b′), (c′–d′), (e′–f′), (g′–h′) on curves *2* Figure 7, *b* and *c* mean that twins are not separated in these regions and J_{cg}, J_{cp}, J_{ceff} values are maintained. Difference of J_{ceff} values on curves *1* and *2* Figure 7 is caused by different initial values of J_c and *d* for samples No. 1 and 2.

Figure 8 for samples No. 1 (curve *1*) and No. 2 (curve *2*) show current dependences representing the difference of J_c and J_{ceff} measured using the four-probe scheme and by magnetic measurements, respectively: *a*) $(J_c - J_{ceff})(H_{ic1})$; *b*) $(J_c - J_{ceff})(J_{cg})$ and *c*) $(J_c - J_{ceff})(1/d)$. J_{ceff} is governing in $J_c - J_{ceff}$. Therefore, growth of J_{ceff} in Figure 7 results in decline of $J_c - J_{ceff}$, qualitative maintenance of the type of plateau and dip on curves *1* and *2* Figure 8. Thus, as the findings show, relation of currents (8) influences the occurrence of growth, decline areas and plateaus, change in their length, linear sections with knees of dependences shown in Figures 7 and 8. Relation (8) also influences different behavior of curves *1* and *2* for sample No. 1 and curves *3* and *4* for sample No. 2 Figure 2, *b*.

Substituting J_{ceff} and J_{cg} values into (8) for J_{cp} with field $\sim 8 \cdot 10^{-2}$ T, we get $\sim 10^9$ A/m^2, which agrees well with the intragrain currents described in literature.

As shown in Figure 8, *a* and equation (8), for samples No. 1 and 2 with field $\sim 8 \cdot 10^{-2}$ T, H_D and H_{Dtr} suppress J_c at $\sim$ 70samples with high J_c, such current drop constitute a considerable proportion of the current reduction during magnetic transport measurements. According to literature data, field $\sim 10^{-2}$ T by more than two orders of magnitude suppresses J_c with $\sim 5 \cdot 10^7$ A/m^2. As shown in Figure 8 *v,g*, $J_c - J_{ceff}$ decreases with growth of J_{cg} and decrease of *d*. However, according to Figure 5, *b*, J_{cg} grows with decreasing *d*, and this results in the fact that the impact of image currentJ_{cg} on J_c becomes greater and, as mentioned above, with decrease of *d* the influence of J_{cg} becomes even greater due to reduction of the number of TBs inside twins. In [15,16] without considering the influence of H_D and H_{Dtr} on J_c, it is shown that low J_{cg} and *d* values result in the increase of J_c, because the influence of pinning inside twins and in the intertwin space

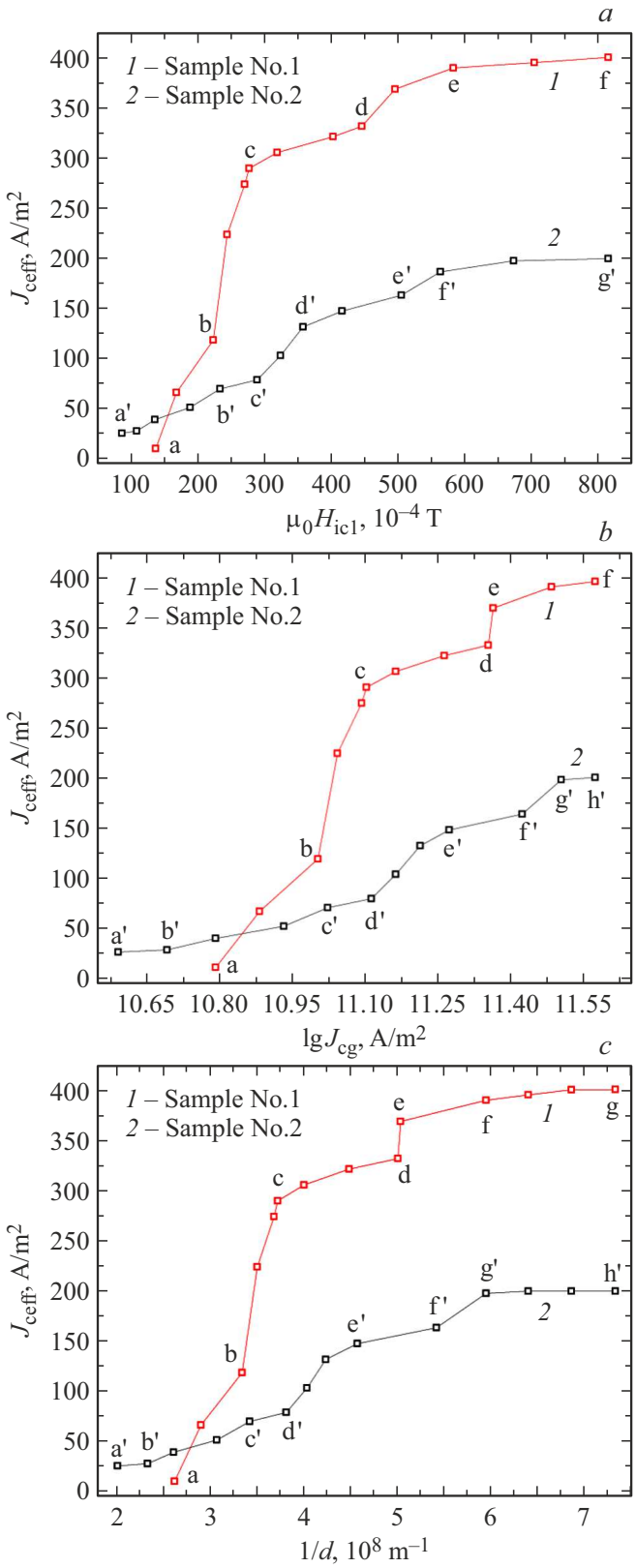

Figure 7. Dependences of critical rms current of twins: *a*) $J_{ceff}(H_{ic1})$; *b*) $J_{ceff}(J_{cg})$ and *c*) $J_{ceff}(1/d)$. Curve *1* — for sample No. 1, curve *2* — for sample No. 2. $T = 77.4$ K.

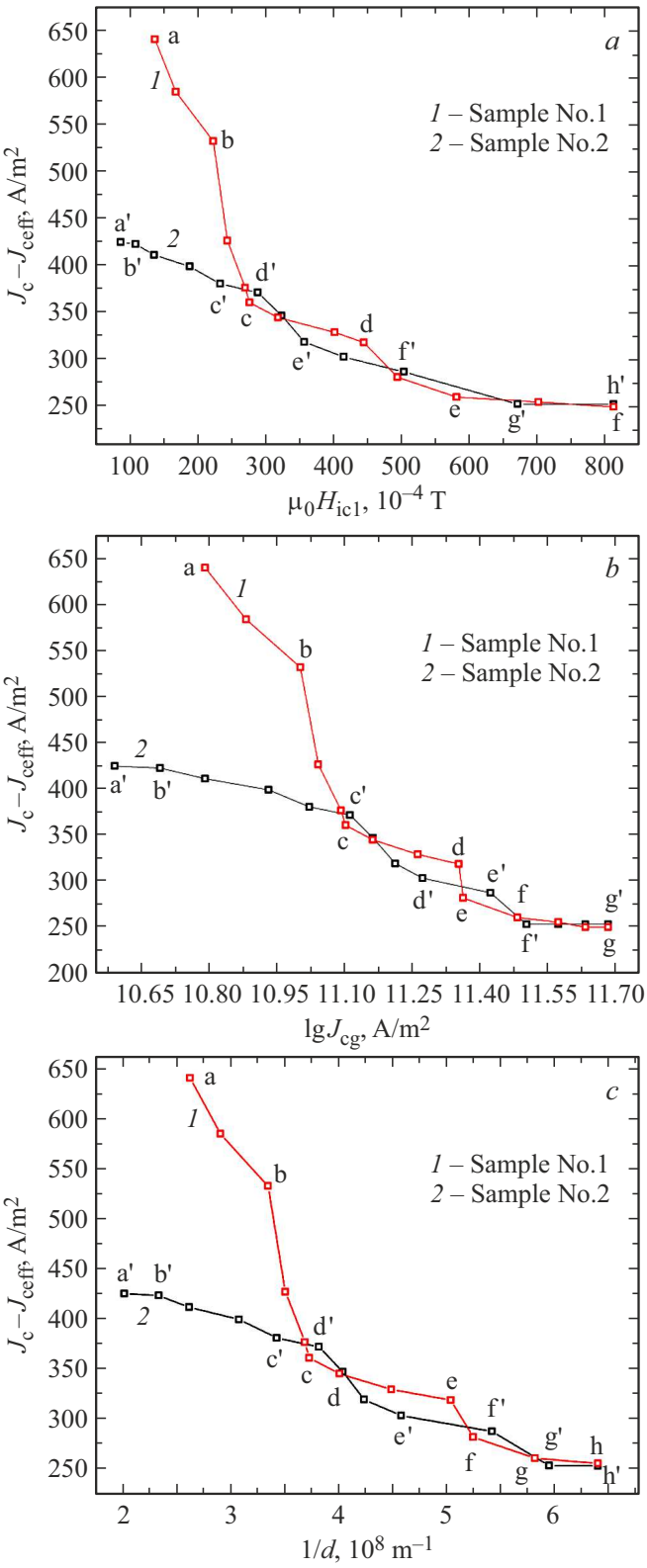

Figure 8. Dependences of the difference of currents J_c and J_{ceff} measured according to the four-probe scheme and magnetic measurements, respectively: *a*) $(J_c - J_{ceff})(H_{ic1})$; *b*) $(J_c - J_{ceff})(J_{cg})$ and *c*) $(J_c - J_{ceff})(1/d)$. Curve *1* — for sample No. 1, curve *2* — for sample No. 2. $T = 77.4$ K.

increases with decreasing d. To check this statement, we initially took the samples with lower d values and high J_c (sample No. 1) and samples with high d values and low J_c (sample No. 2). As follows from the findings shown in Figures 7 and 8, with increasing J_{cg} (as in [15,16]), J_c decreases, and decreasing d results in J_c decrease, rather than in increase. This result is also confirmed by the fact that J_{cg} and J_{ceff}, on the one hand, increase due to the lower number of TBs within the twins with field growth when larger twins are disintegrated into smaller twins with close n, and as a result J_c decreases; on the other hand, as shown in Figure 5, *b* and Figure 8, *b* and *c*, the influence of J_{cg} and J_{ceff} on J_c becomes higher with lower influence of H_{Dtr} due to decreasing n of the twins because of their smaller sizes. Thus, it is required to correct the findings of [15,16] considering the facts of considerable influence of H_D and H_{Dtr} on J_c. As the findings show, the offered uniformly magnetized sample model, in contrast with the corrected analytical and generalized Bean critical state models, allows to determine unambiguously not only intertwin, intratwin, Meissner critical image currents, thermodynamic first critical magnetic fields of twins, linear dimensions of twins, effective demagnetizing factor of the sample during field penetration in the sample, etc., but also to describe physical processes in such complex, naturally formed Josephson media as HTSC materials. In addition, since, with field growth, stepwise disintegration of larger twins into smaller twin groups takes place, which are, in turn, sorted by close demagnetizing factors, currents J_{cg}, J_{cp} and intertwin Josephson coupling energies between them, then the Bean model can be implemented according to these parameters inside each particular isolated twin group. Further field growth will result in disintegration of these twins into relatively smaller twins with higher coupling energies and currents J_{cg}, J_{cp}. The bean model can be also implemented within the formed groups, and transition from the twins with low parameters to the twins with higher parameters will take place, etc. Nanocrystalls that do not have TB inside them have the highest intertwin Josephson coupling energy. Thus, according to the findings, HTSC materials are a multistep system and, therefore, the Bean model is not observed on the macroscopic sample due to gradual stepwise suppression of the intertwin Josephson coupling energy. So, to describe the magnetic properties of HTSC throughout the magnetic field and current range using the generalized Bean model, the full range of Bean models describing field and current distributions within particular isolated twins with their dimensions, critical currents and fields shall be „sewn“ together. Thus, unambiguous determination of critical currents using the Bean model in such complex Josephson HTSC medium that varies with field variation is a difficult and sometimes unsolvable task. The findings also show that the Bean model can be used to describe spatial distribution of current and field in the HTSC material in the field region below the first critical magnetic field of twins. Taking into account the fact that a superconducting circuit hierarchy with various critical

currents, fields and n is formed in the weak field region, the uniformly magnetized sample model is applicable to description of the magnetic properties of the HTSC material throughout the field and current range.

5. Conclusion

The influence of twin demagnetization fields on physical processes in a HTSC sample and its twins was studied by exposure of polycrystalline and quasi-single-crystalline twin YBCO samples with various dimensions and critical currents to the oscillating local evanescent magnetic field. The role of the demagnetization fields of the sample H_D and twins H_{Dtr} in formation of macroscopic and local fundamental parameters of the YBCO samples was identified. It is shown that in the field range $\sim (1-60) \cdot 10^{-4}$ T, standardized axial distribution of the residual current is well described within the Bean critical state model, and in the range $\sim (1-800) \cdot 10^{-4}$ T — within the uniformly magnetized sample model. Such result is also confirmed during current flow through the sample perpendicular to the force lines of the magnetic field. The offered model explains the retransformation of physical processes in HTSC under the influence of H_D and H_{Dtr} in the uniformly magnetized sample with isolated twins. When the oscillating local evanescent magnetic field is applied, Meissner image currents J_{cg} flow on the twin surfaces and induce demagnetization fields oriented against the demagnetization fields associated with the vortex scattering fields supported by the intratwin pinning currents J_{cp}. Thus, H_D and the resulting field H_{Dtr} suppress the critical currents J_c through the intertwin weak couplings and cause disintegration of large twins into smaller isolated uniformly magnetized twins with currents J_{ceff}. With field $\sim 8 \cdot 10^{-2}$ T, $J_{cp} \approx 10^9$ A/m^2 is obtained, which agrees well with the intragrain currents described in the literature. The findings may be also extended to other „multicoupling“ twin-structured superconductors with different properties and morphology.

Funding

This study was financed from the budget under the state assignment of Kotel'nikov Institute of Radio Engineering and Electronics of the Russian Academy of Sciences.

Conflict of interest

The authors declare that they have no conflict of interest.

References

[1] S. Nakahara, M.F. Boone, G.J. Fisanick Yan, D.W. Johnson. J. Appl. Phys. *63*, *2*, 451 (1988).
[2] A.A. Abrikosov, A.I. Buzdin, M.L. Kulic, D.A. Kuptsov. JETP **68**, *1*, 210 (1989).
[3] Kh.R. Rostami. JETP Lett. **108**, *11*, 734 (2018).
[4] Chemistry of High-Temperature Superconductors / Eds. D.L. Nelson, M.S. Whittingham, T.F. George. Am. Chem. Soc., Washington, DC (1987).
[5] Physical Properties of High-Temperature Superconductors / Ed. D.M. Ginsberg. World Sciientific, Singapore (1990).
[6] B. Kalisky, J.R. Kirtley, J.G. Analytis, J.-H. Chu, I.R. Fisher, K.A. Moler. Phys. Rev. B *83*, *6*, 064511 (2011).
[7] Kh.R. Rostami. Int. J. Mod. Phys. B **32**, *31*, 1850346 (2018).
[8] D.M. Gokhfeld. Phys. Solid State **56**, *12*, 2380 (2014).
[9] A.A. Elistratov, I.L. Maksimov. Phys. Solid State **42**, *2*, 201 (2000).
[10] C.P. Bean. Rev. Mod. Phys. **36**, *1*, 31 (1964).
[11] Kh.R. Rostami. ZHTF **90**, *12*, 2066 (2020). [Tech. Phys. **65**, *12*, 1975 (2020)].
[12] Kh.R. Rostami. PTE, **2**, *112* (2016) (in Russian).
[13] M. Tinkham. Introduction to superconductivity. McGraw-Hill (1975).
[14] E.A. Linton. Superconductivity. Methuen, London (1964).
[15] V.M. Svistunov, A.I. D'yachenko. Supercond. Sci. Technol. **5**, *2*, 98 (1992).
[16] J. Hecher, T. Baumgartner, J.D. Weiss, C. Tarantini, A. Yamamoto, J. Jiang, E. Hellstrom, D. Larbalestier, M. Eisterer. Supercond. Sci. Technol. *29*, *2*, 025004 (2016).

Translated by E.Ilyinskaya